REVISTA MATÉRIA V.30
ISSN 1517-7076 articles e20250108, 2025

Investigation of graphene/$Ti_3C_2T_x$ transition-metal carbide composite coatings for steel surface protection

Min Yuan

[1]Anhui Technical College of Industry and Economy, School of Continuing Education. 230061, Hefei, Anhui, China.
e-mail: 13955110578@163.com

ABSTRACT

This study developed and systematically investigated a novel protective coating system combining graphene oxide (GO) and $Ti_3C_2T_x$ for enhanced steel surface protection. Through careful optimization of synthesis parameters and composition ratios, we achieved uniform dispersion and strong interfacial interactions between the components, resulting in a dense, well-adhered coating structure. The composite exhibited exceptional mechanical properties, with nanoindentation measurements revealing uniform distribution of hardness (coefficient of variation <8%) across the coating surface. Electrochemical analysis demonstrated the coating's remarkable barrier properties, with impedance measurements showing charge transfer resistance values exceeding 10^9 $\Omega \cdot cm^2$ in 3.5 wt% NaCl solution. The coating maintained structural integrity and protective performance during prolonged environmental exposure, retaining over 85% of its initial adhesion strength after 30 days under accelerated aging conditions. Potentiodynamic polarization studies revealed a significant reduction in corrosion rate, with the corrosion current density decreasing by three orders of magnitude compared to unprotected steel. The optimized coating system demonstrated excellent long-term stability in salt spray testing, maintaining a high corrosion rating throughout 1000 hours of exposure, indicating its potential for practical industrial applications.

Keywords: Anticorrosion performance; Electrochemical impedance; Nanocomposite materials; Barrier properties; Mechanical durability.

1. INTRODUCTION

Metal corrosion represents one of the most significant challenges facing modern infrastructure and industrial systems, leading to substantial economic losses and safety concerns across various sectors. The deterioration of steel surfaces, in particular, has prompted extensive research into protective coating technologies that can effectively prevent or minimize corrosion damage while maintaining structural integrity [1–3]. Traditional protective coatings, while functional, often suffer from limitations such as poor adhesion, inadequate barrier properties, and susceptibility to mechanical damage under harsh environmental conditions. Recent advances in materials science have opened new avenues for developing high-performance protective coatings through the incorporation of two-dimensional (2D) nanomaterials [4]. Among these, two-dimensional transition-metal carbide/nitride (MXenes) and graphene oxide (GO) have emerged as promising candidates for corrosion protection due to their unique structural and chemical properties. MXenes, a family of 2D transition metal carbides and nitrides, exhibit remarkable mechanical strength, high electrical conductivity, and excellent chemical stability [5–7]. Their accordion-like lamellar structure provides an effective barrier against corrosive agents, while their surface chemistry can be readily modified to enhance compatibility with various coating matrices [8, 9].

The integration of graphene oxide with MXenes presents an innovssative approach to addressing the inherent limitations of single-component protective coatings [10]. Graphene oxide, characterized by its atomically thin structure and abundant oxygen-containing functional groups, offers complementary properties to MXenes [11, 12]. The synergistic combination of these materials can potentially yield superior coating performance through multiple mechanisms: enhanced barrier properties, improved mechanical strength, and better adhesion to metallic substrates [13–15]. However, the development of effective GO-MXene composite coatings faces several challenges. The oxidation susceptibility of MXenes in ambient conditions can compromise their long-term stability and protective capabilities [16, 17]. While previous studies, such as the work by CAO *et al.*

Corresponding Author: Min Yuan Received on 01/02/2025 Accepted on 24/06/2025

DOI: https://doi.org/10.1590/1517-7076-RMAT-2025-0108

[18], have explored MXene-based multilayer coatings with silane modifiers on aluminum substrates, the novelty of this study lies in its development of a GO–$Ti_3C_2T_X$ composite coating optimized for carbon steel protection without polymeric binders. This binder-free dual-lamellar system achieves a unique combination of superior mechanical hardness (4.8 ± 0.3 GPa), high adhesion strength (18.5 ± 0.8 MPa), and long-term corrosion resistance, including salt spray durability and electrochemical performance. Furthermore, we elucidate the interfacial mechanisms that contribute to these properties, offering insights not previously detailed in GO/MXene coating literature [19–21]. Additionally, achieving uniform dispersion and strong interfacial interactions between the components is crucial for optimal coating performance [22, 23]. The control of coating thickness and microstructure also plays a vital role in determining the final protective properties [24].

This research introduces a novel approach to fabricating GO–$Ti_3C_2T_x$ composite coatings for steel surface protection. The study focuses on understanding the fundamental mechanisms governing the enhanced protective properties of these composite coatings and establishing structure-property relationships. By carefully controlling the synthesis parameters and optimizing the coating composition, we aim to develop a robust protective system that combines the advantages of both materials while mitigating their individual limitations. The selection of $Ti_3C_2T_x$ as the MXene component is based on its excellent mechanical properties, good chemical stability, and well-established synthesis protocols [25]. When combined with graphene oxide, the resulting composite is expected to form a dense, well-adhered coating with superior barrier properties [26]. The presence of oxygen-containing functional groups on both components facilitates strong interfacial interactions and enables better integration with the substrate surface.

2. MATERIALS AND METHODS

High-purity Ti_3AlC_2 layered $M_{n+1}AX_n$ (MAX) phase powder (98.5% purity, 300 mesh) was obtained from Shanghai Advanced Materials Co., Ltd. (Shanghai, China). Lithium fluoride (LiF, analytical grade) and hydrochloric acid (HCl, 37 wt%) were purchased from Beijing Chemical Works (Beijing, China). Natural graphite flakes (99.9% purity, 325 mesh) were supplied by Qingdao Huatai Lubricant Sealing S&T Co., Ltd. (Qingdao, China). Potassium permanganate ($KMnO_4$), sulfuric acid (H_2SO_4, 98%), hydrogen peroxide (H_2O_2, 30%), and ethanol (analytical grade) were acquired from Sinopharm Chemical Reagent Co., Ltd. (Shanghai, China). Q235 steel substrates (50 mm × 50 mm × 2 mm) were provided by Baowu Steel Group Corporation (Shanghai, China).

$Ti_3C_2T_x$ MXene was synthesized through selective etching of Ti_3AlC_2 MAX phase [27, 28]. Typically, 2.0 g of Ti_3AlC_2 powder was gradually added to a solution containing 40 mL of 9M HCl and 3.2 g LiF under continuous stirring. The mixture was maintained at 35°C for 24 hours in an oil bath with magnetic stirring at 400 rpm. The resulting suspension was centrifuged at 3500 rpm for 5 minutes and washed repeatedly with deionized water until the supernatant reached pH 6. The obtained Ti3C2Tx was then dispersed in deionized water through sonication for 1 hour to achieve delamination.

Graphene oxide was synthesized using a modified Hummers method [29]. Briefly, 2.0 g of graphite flakes were added to 46 mL of concentrated H_2SO_4 under ice-bath conditions. Subsequently, 6.0 g of $KMnO_4$ was slowly added while maintaining the temperature below 20°C. The mixture was stirred at 35°C for 2 hours, followed by dilution with 92 mL of deionized water. After stirring for an additional 15 minutes, the reaction was terminated by adding 280 mL of deionized water and 20 mL of H_2O_2 solution. The product was washed repeatedly with deionized water through centrifugation until neutral pH was achieved.

The composite coating was prepared by combining $Ti_3C_2T_x$ and GO suspensions in a 2:1 mass ratio. The mixed suspension was sonicated for 30 minutes to ensure homogeneous distribution. Prior to coating application, Q235 steel substrates were mechanically polished using successive grades of SiC papers (400–2000 grit), followed by ultrasonic cleaning in acetone, ethanol, and deionized water. The substrates were then dried under nitrogen flow. The composite suspension was spray-coated onto the prepared substrates using a programmable spray coater (Model XDC-100, Xindao Instrument, Nanjing, China) with the following parameters: nozzle distance 15 cm, spray pressure 0.2 MPa, substrate temperature 80°C, and flow rate 2 mL/min.

The morphology and microstructure of the coatings were examined using a field emission scanning electron microscope (FESEM, JSM-7800F, JEOL, operated at 5 kV). X-ray diffraction (XRD) patterns were recorded using a Rigaku SmartLab diffractometer with Cu Kα radiation (λ = 1.5418 Å). Raman spectra were collected using a Renishaw inVia spectrometer with 532 nm laser excitation. X-ray photoelectron spectroscopy (XPS) analysis was performed using a Thermo Scientific ESCALAB 250Xi system.

Coating adhesion was evaluated using a digital pull-off adhesion tester (PosiTest AT-A, DeFelsko) following the ASTM D4541 standard. The coating thickness was measured using a magnetic thickness gauge (TT260, Time Group Inc.). Nanoindentation tests were conducted using a Hysitron TI 950 TriboIndenter with a Berkovich diamond tip at a maximum load of 10 mN. Prior to coating deposition, the as-polished Q235 steel

substrates (Ra ≈ 18 nm) were tested under the same conditions, yielding a baseline hardness (H_{sub}) of 1.56 ± 0.05 GPa and elastic modulus (E_{sub}) of 211 ± 6 GPa. This baseline permits a direct quantitative comparison with the composite coating, as recommended by ATAIE *et al.* [30, 31].

Electrochemical measurements were performed using a CHI760E electrochemical workstation in a three-electrode cell configuration. A platinum plate served as the counter electrode, and a saturated calomel electrode (SCE) was used as the reference electrode. Electrochemical impedance spectroscopy (EIS) was conducted at open circuit potential with a frequency range of 100 kHz to 10 mHz and an AC amplitude of 10 mV. All spectra were fitted with ZView 4.0 using a Rs(QcRc)(QdlRct) equivalent-circuit. Fitting quality was verified by $\chi^2 \leq 1 \times 10^{-3}$ and weighted residuals below 5% across the entire frequency range. The salt spray test was carried out in a salt spray chamber (YWX/Q-750, Jinghong Test Equipment) according to the ASTM B117 standard using 5 wt% NaCl solution at 35°C.

To assess the reproducibility of the coating fabrication and performance results, all key experimental measurements were conducted on at least three independently prepared samples per coating condition. For each set, separate batches of GO–$Ti_3C_2T_X$ coatings were synthesized and applied under the same processing conditions. Adhesion strength, mechanical properties, electrochemical impedance spectra, and polarization curves were independently measured for each sample. Mean values along with standard deviations were reported to reflect data consistency. The low coefficients of variation (typically below 8%) for key parameters such as hardness, impedance modulus, and corrosion current density confirm the high reproducibility of the fabrication method and the robustness of the composite coating system.

3. RESULTS AND DISCUSSION

The morphological characteristics of the GO–$Ti_3C_2T_x$ composite coating were investigated using electron microscopy techniques. Figure 1a presents the SEM micrograph of the as-deposited coating surface, revealing a uniform layered structure with overlapping sheets of GO and $Ti_3C_2T_x$. The $Ti_3C_2T_X$ platelets, appearing as brighter regions due to their higher atomic number, demonstrate typical accordion-like morphology with lateral dimensions ranging from 2–5 μm. This platelet size, in combination with wrinkled GO sheets, contributes to a finely structured, interleaved lamellar architecture. Smaller grain features and compact layering enhance the tortuosity of diffusion pathways and reduce microvoid formation, both of which play a critical role in mitigating ion permeation and corrosion initiation. Grain refinement is also known to promote passivation by increasing grain boundary density, thereby enhancing coating stability and corrosion resistance [32]. These platelets are observed to be well-integrated with the darker GO sheets, which exhibit wrinkled features characteristic of graphene oxide structures [33]. In addition, Energy Dispersive X-ray Spectroscopy (EDS) was performed to confirm the elemental composition and distribution within the composite coating. As shown in Figure 1c–f, the EDS mapping reveals the presence of carbon (C), oxygen (O), titanium (Ti), and fluorine (F), which are consistent with the elemental constituents of GO and $Ti_3C_2T_X$. The uniform spatial distribution of these elements across the scanned area confirms the homogeneous dispersion and successful integration of the two components within the composite matrix.

XRD analysis (Figure 2a) comparatively illustrates the diffraction patterns of pristine GO, $Ti_3C_2T_X$, and the GO–$Ti_3C_2T_X$ composite coating. The characteristic (002) reflection of $Ti_3C_2T_X$ appears at $2\theta = 6.5°$, consistent with typical MXene structure [34]. In contrast, pristine GO shows a broad (001) peak centered at $2\theta \approx 11.2°$, confirming its oxidized layered structure and the absence of the graphite (002) peak at 26.5°. Upon composite

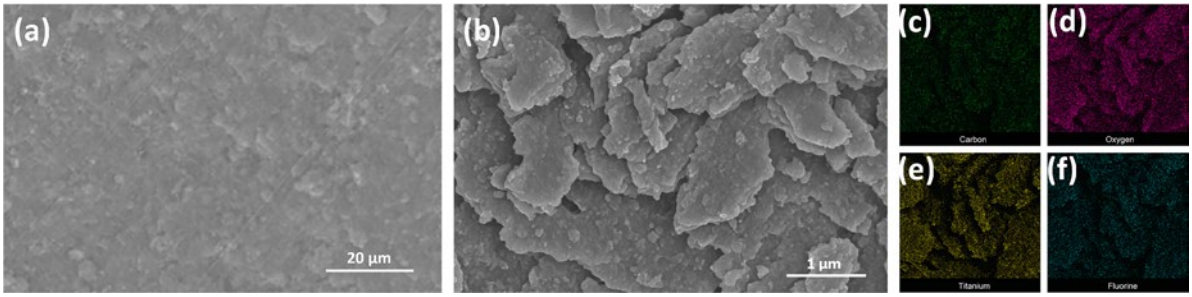

Figure 1: SEM of GO–$Ti_3C_2T_x$ composite coating with (a) low magnification and (b) high magnification. EDS elemental mapping of the GO–$Ti_3C_2T_X$ composite coating showing the distribution of (c) carbon, (d) oxygen, (e) titanium, and (f) fluorine. The uniform dispersion supports effective compositional integration.

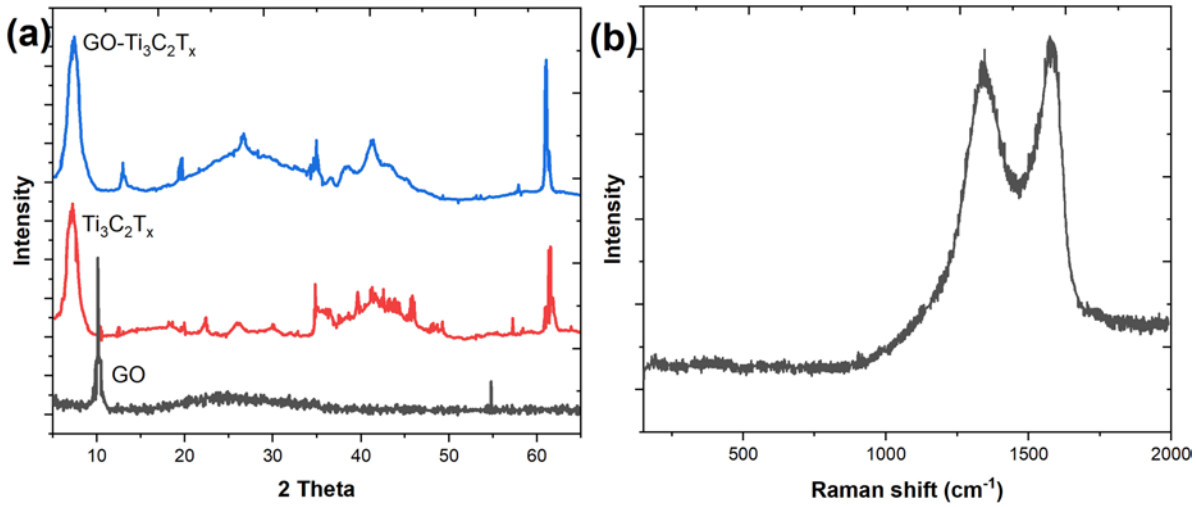

Figure 2: Structural characterization of GO–$Ti_3C_2T_x$ composite coating. (a) XRD patterns showing characteristic peaks of constituent phases. (b) Raman spectra highlighting vibrational modes of both components and their interactions.

formation, the GO–$Ti_3C_2T_X$ pattern exhibits a slight shift and broadening of the (002) peak to $2\theta \approx 6.8°$. Based on Bragg's law, the interlayer spacing (d-spacing) for pristine $Ti_3C_2T_X$ is calculated as 1.36 nm ($2\theta = 6.5°$), which decreases slightly to 1.30 nm for the GO–$Ti_3C_2T_X$ composite ($2\theta = 6.8°$). This marginal reduction, rather than increase, in interlayer distance suggests structural compaction, potentially due to partial GO reduction and restacking during composite formation. These findings refine our earlier interpretation and indicate that GO incorporation leads to structural reorganization rather than pure interlayer expansion. These results indicate strong physical interactions and structural reorganization between the two components during the composite preparation. Raman spectroscopy (Figure 2b) provides further evidence of the chemical interactions between the components. The spectrum exhibits characteristic D and G bands of GO at 1350 and 1580 cm^{-1}, respectively, alongside the typical $Ti_3C_2T_x$ vibration modes at 200, 400, and 600 cm^{-1}. The intensity ratio of D to G bands ($I_D/I_G = 0.92$) suggests partial reduction of GO during the composite formation process [35].

The adhesion strength between the GO–$Ti_3C_2T_x$ composite coating and steel substrate was evaluated through pull-off tests under various conditions. Figure 3a presents the adhesion strength measurements for coatings with different GO:$Ti_3C_2T_x$ ratios. The optimal composition (2:1 ratio) exhibited a remarkable adhesion strength of 18.5 ± 0.8 MPa under normal conditions, outperforming silane-wrapped GO@MXene/epoxy films (14.2 MPa) [36] and polyimide/MXene layers (12.1 MPa) [37] measured on mild-steel substrates by the same ASTM D4541 protocol. The enhanced adhesion is attributed to the synergistic effect of oxygen-containing functional groups from both components interacting with the steel substrate [38, 39].

The durability of adhesion strength was assessed under various environmental conditions (Figure 3b). After 30 days of exposure to 95% relative humidity at 40°C, the composite coating maintained 85% of its initial adhesion strength, demonstrating superior environmental stability compared to single-component coatings.

Nanoindentation measurements revealed the mechanical robustness of the composite coating. Figure 4 shows representative load-displacement curves for the composite coating compared to pure components. The GO–$Ti_3C_2T_X$ composite exhibited a maximum hardness of 4.8 ± 0.3 GPa and elastic modulus of 78.5 ± 2.1 GPa, corresponding to a 210% increase over the uncoated Q235 substrate (Hsub = 1.56 ± 0.05 GPa). The hardness ratio (Hcoat/H_sub ≈ 3.1) falls within the range reported for Cr-Nb-Ti-Zr-N-O nanocomposite and Ti/TiCrN bilayer coatings (3–6 × enhancement) that were highlighted by KOSARI MEHR *et al.* [40], confirming the mechanical relevance of the current system (Table 1). These results confirm the significant enhancement achieved through compositing. The spatial distribution of mechanical properties across the coating surface demonstrated strong uniformity, with the coefficient of variation (CV) calculated at 6.3% for hardness and 7.2% for elastic modulus (n = 10). This suggests homogeneous load distribution and consistent structural integrity, reflecting the uniform dispersion of GO and $Ti_3C_2T_X$ in the matrix [41]. This uniformity confirms the homogeneous integration of the components and suggests effective load distribution throughout the coating structure.

AFM measurements (Figure 5) provided detailed insight into surface topography and mechanical uniformity at the nanoscale. The GO–$Ti_3C_2T_X$ composite coating exhibited an RMS roughness of 14.8 nm, significantly

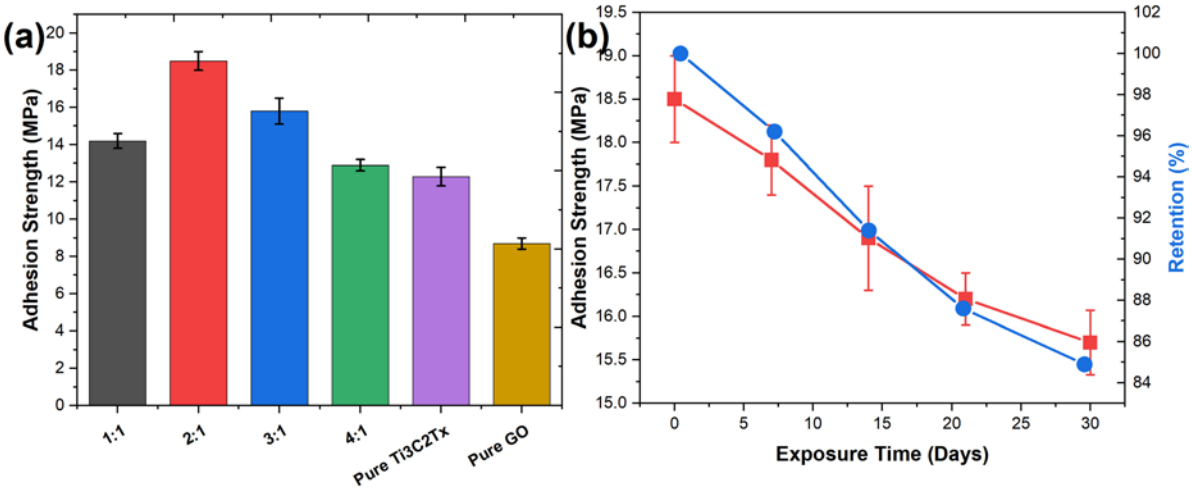

Figure 3: Adhesion performance of GO–$Ti_3C_2T_x$ composite coating. (a) Pull-off adhesion strength as a function of composition ratio. (b) Environmental stability of adhesion strength under various conditions. Error bars represent standard deviation from five measurements.

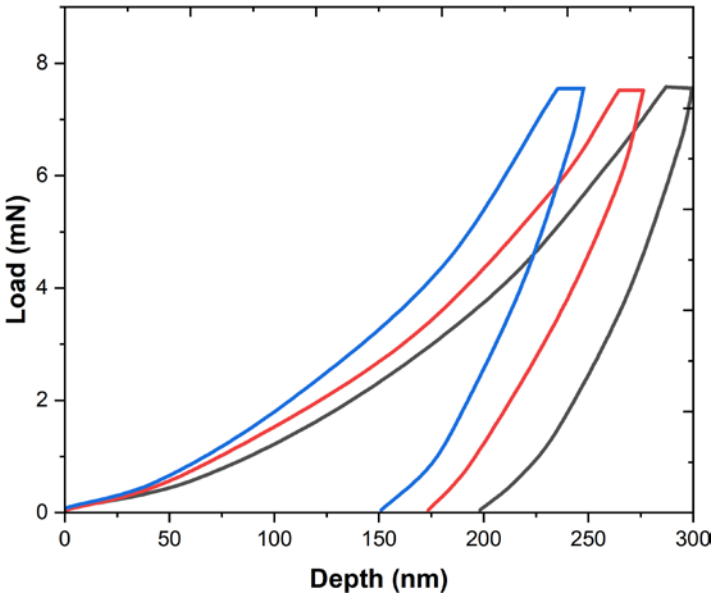

Figure 4: Representative load–displacement curves for GO, $Ti_3C_2T_X$, and GO–$Ti_3C_2T_X$ composite coatings obtained from nanoindentation measurements.

Table 1: Comparison of mechanical properties between composite and single-component coatings.

SAMPLE	HARDNESS (GPa)	ELASTIC MODULUS (GPa)	ADHESION STRENGTH (MPa)
GO–$Ti_3C_2T_x$	4.8 ± 0.3	78.5 ± 2.1	18.5 ± 0.8
$Ti_3C_2T_x$	3.2 ± 0.2	65.3 ± 1.8	12.3 ± 0.7
GO	1.8 ± 0.2	42.1 ± 1.5	8.7 ± 0.5

lower than that of $Ti_3C_2T_X$ (22.3 nm) and GO (27.6 nm) coatings. Corresponding PeakForce modulus maps demonstrated a homogeneous stiffness distribution, further corroborating the uniform load-bearing capability of the composite film. These nanoscale observations reinforce the nanoindentation results and highlight the compactness and interfacial cohesion achieved through composite formation. Similar nanoscale mechanical

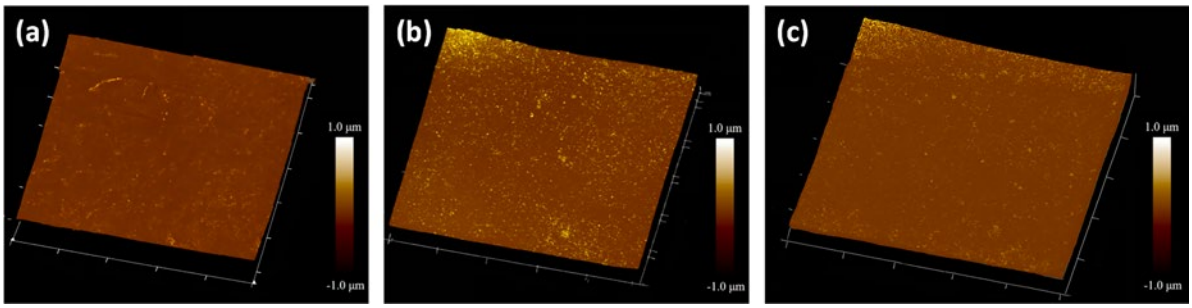

Figure 5: AFM topography images of (a) GO coating, (b) $Ti_3C_2T_X$ coating, and (c) GO–$Ti_3C_2T_X$ composite coating.

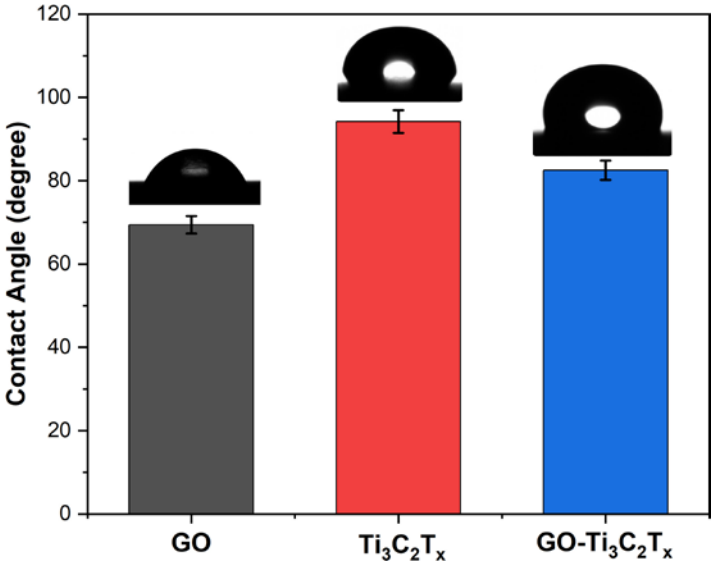

Figure 6: Static water contact angle measurements for GO, $Ti_3C_2T_X$, and GO–$Ti_3C_2T_X$ coatings. Results demonstrate intermediate wettability for the composite coating.

reinforcement through topographical refinement has been reported in previous studies on multilayer ceramic and metallic thin films [40].

The surface wettability of the coatings was evaluated by measuring the static water contact angle. Figure 6 presents the representative contact angle images for GO, $Ti_3C_2T_x$, and GO–$Ti_3C_2T_x$ composite coatings. The pure GO coating exhibited a contact angle of 69.4° ± 2.1°, indicating a hydrophilic surface due to the presence of abundant oxygen-containing functional groups. In contrast, the pure $Ti_3C_2T_x$ coating showed a more hydrophobic behavior with a contact angle of 94.2° ± 2.7°, consistent with its surface termination groups and relatively lower oxygen content. The GO–$Ti_3C_2T_x$ composite coating demonstrated a moderate hydrophilicity, with a contact angle of 82.5° ± 2.3°. This intermediate wettability can be attributed to the synergistic combination of hydrophilic GO and relatively hydrophobic $Ti_3C_2T_x$ components, resulting in a balanced surface energy. The moderately hydrophilic character of the composite surface is favorable for corrosion protection, as it reduces the adhesion and permeation of corrosive aqueous solutions while maintaining strong adhesion with the metallic substrate. It closely matching the 80–85° window reported for self-healing GO/MXene/PDA films that showed optimum anti-salt performance [42].

The influence of coating thickness on mechanical performance was systematically investigated. Figure 7 demonstrates the relationship between coating thickness and key mechanical parameters. Quantitative analysis of coating thickness revealed that the 3.0–3.5 µm range exhibited peak performance in both mechanical adhesion and corrosion resistance. Adhesion values averaged 18.5 ± 0.8 MPa with minimal variation (±4.3%).

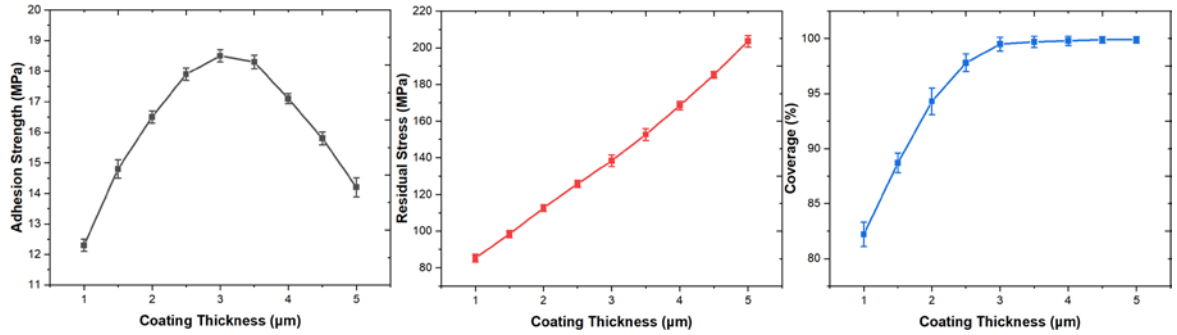

Figure 7: Coating thickness optimization. (a) Correlation between coating thickness and mechanical properties.

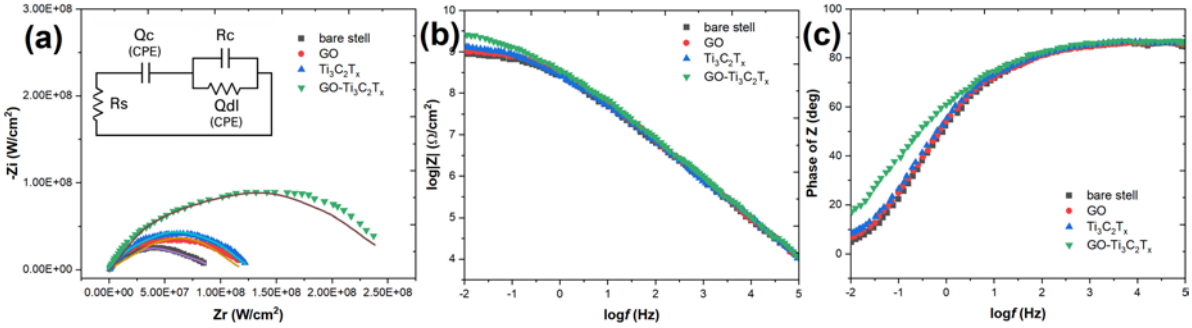

Figure 8: EIS analysis of different coatings in 3.5 wt% NaCl solution. (a) Nyquist plots, (b) Bode magnitude plots, and (c) Bode phase angle plots. Inset shows the equivalent circuit model used for data fitting.

Electrochemical impedance spectroscopy (EIS) and salt spray tests corroborated these findings, showing that coatings within this optimal thickness range exhibited the highest impedance modulus ($|Z|_{0.01}$Hz) and lowest corrosion current density. In contrast, thinner films (<2.0 μm) suffered from incomplete substrate coverage, allowing localized electrolyte penetration and increased corrosion activity. Thicker coatings (>4.0 μm), while initially dense, were prone to internal stress accumulation and microcrack formation, which facilitated moisture ingress and led to premature degradation under extended salt spray exposure. These findings emphasize the critical role of thickness optimization not only for mechanical durability but also for achieving robust and long-lasting corrosion protection. Coatings thinner than 2.0 μm showed insufficient surface coverage, while those exceeding 4.0 μm exhibited decreased adhesion strength due to increased residual stresses [43].

Electrochemical impedance spectroscopy (EIS) was employed to evaluate the corrosion protection performance of the c composite coating. Figure 8 presents the Nyquist and Bode plots obtained in 3.5 wt% NaCl solution. The composite coating exhibited significantly larger impedance modulus (|Z|) values compared to bare steel and single-component coatings. At low frequencies (0.01 Hz), the |Z| value for GO–$Ti_3C_2T_x$ reached 2.3×10^9 Ω·cm², approximately two orders of magnitude higher than that of pure $Ti_3C_2T_x$ (3.5×10^7 Ω·cm²) and GO (1.8×10^7 Ω·cm²) coatings. The phase angle plots showed two distinct time constants, indicating the formation of a stable passive layer [44]. Inset of Figure 7a displays the physical equivalent circuit used for data fitting, consisting of solution resistance (R_s), a constant-phase element representing the intact coating (Qc) in parallel with coating resistance (R_c), and a second CPE for the double layer (Qdl) in parallel with charge-transfer resistance (Rct) [45]. The GO–$Ti_3C_2T_X$ composite coating exhibited a coating resistance (R_c) of 2.1×10^9 Ω·cm² and a charge transfer resistance (R_{ct}) of 1.5×10^9 Ω·cm², as fitted using the $Rs(Q_cR_c)(Q_{dl}R_{ct})$ equivalent circuit model (Figure 7 inset). Compared to $Ti_3C_2T_X$ ($R_c = 1.4 \times 10^8$ Ω·cm², $R_{ct} = 9.3 \times 10^7$ Ω·cm²) and GO ($R_c = 9.7 \times 10^7$ Ω·cm², $R_{ct} = 8.1 \times 10^7$ Ω·cm²), the composite improved electrochemical stability by more than one order of magnitude. The lower CPE values (Q_c and Q_{dl}) also indicated reduced capacitive leakage and improved film compactness. The χ^2 values for circuit fitting were all $<1 \times 10^{-3}$, confirming excellent model

agreement with experimental data [46]. These values corroborate the superior barrier and kinetic inhibition offered by the dual-lamellar architecture [47, 48]. A summary of all fitting parameters is provided in Table 2.

Potentiodynamic polarization curves (Figure 9) demonstrated the superior corrosion resistance of the composite coating. The GO–$Ti_3C_2T_X$ coating showed a positive shift in corrosion potential (E_{corr}) of 285 mV relative to bare steel (−0.373 V vs. −0.658 V). It also exhibited a significantly lower corrosion current density (i_{corr}) of 2.3×10^{-8} A/cm², compared to 4.8×10^{-7} A/cm² for $Ti_3C_2T_X$ and 8.2×10^{-7} A/cm² for GO (Table 3). These results demonstrate the superior corrosion resistance achieved through composite formulation. It surpassing the 210 mV shift reported for $Ti_3C_2T_x$/LDH heterostructured coatings [49] and the 170 mV shift for GO-wrapped MXene thin films [36], indicating a more effective kinetic suppression of anodic dissolution. Table 3 summarizes the key electrochemical parameters derived from the polarization curves. Additionally, the corrosion protection efficiency (PE) of each coating was calculated.

Table 2: Best-fit circuit parameters derived from EIS spectra of bare steel and coated specimens after 24 h immersion in 3.5 wt % NaCl ($\chi^2 \leq 10^{-3}$).

SAMPLE	R_s (Ω cm²)	Q_c (μF sn^{-1} cm^{-2})	n_c	R_c (Ω cm²)	Q_{dl} (μF sn^{-1} cm^{-2})	n_{dl}	R_{ct} (Ω cm²)
Bare steel	18	250	0.86	2.4×10^4	175	0.82	5.8×10^3
GO coating	17	112	0.88	9.7×10^7	64	0.80	8.1×10^7
$Ti_3C_2T_x$ coating	18	89	0.90	1.4×10^8	58	0.81	9.3×10^7
GO–$Ti_3C_2T_x$ composite	17	46	0.92	2.1×10^9	27	0.88	1.5×10^9

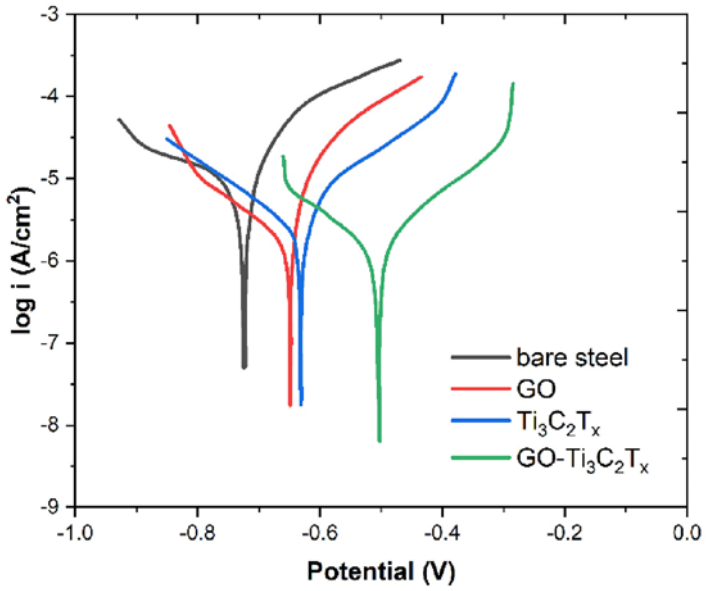

Figure 9: Potentiodynamic polarization curves of bare steel and coated samples in 3.5 wt% NaCl solution showing enhanced corrosion resistance of the composite coating.

Table 3: Electrochemical parameters derived from polarization curves.

SAMPLE	Ecorr (V vs. SCE)	icorr (A/cm²)	βa (V/dec)	βc (V/dec)	PE (%)
Bare Steel	−0.658	2.5×10^{-5}	0.086	0.092	–
GO–$Ti_3C_2T_x$	−0.373	2.3×10^{-8}	0.112	0.098	99.91
$Ti_3C_2T_x$	−0.512	4.8×10^{-7}	0.095	0.089	98.08
GO	−0.489	8.2×10^{-7}	0.091	0.094	96.72

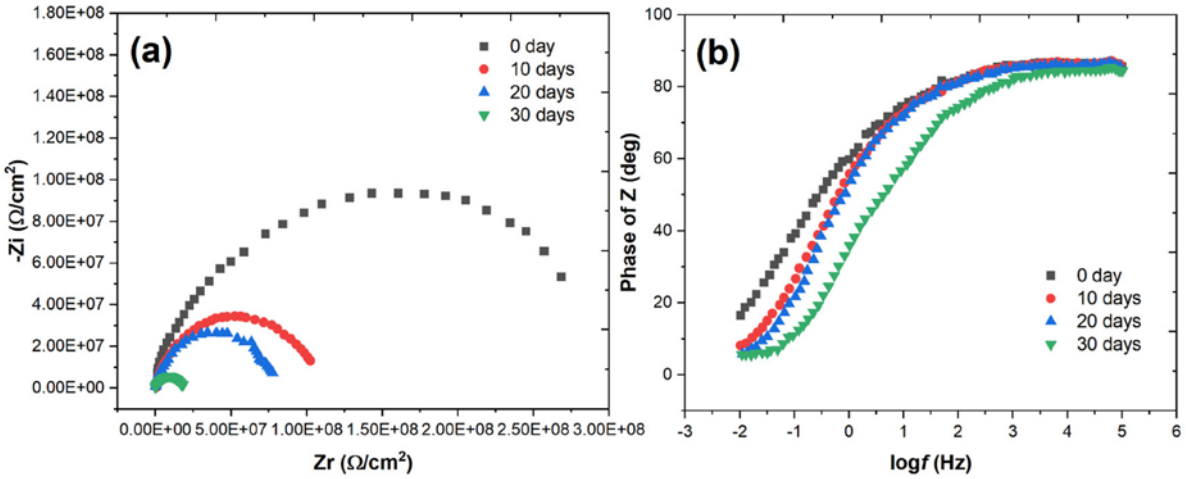

Figure 10: Evolution of (a) impedance modulus and (b) phase angle at 0.01 Hz during 30-day immersion testing.

The long-term stability of the coating was monitored through continuous EIS measurements over 30 days of immersion in 3.5 wt% NaCl solution (Figure 10). The composite coating maintained high impedance values throughout the test period, with less than 15% decrease in |Z|0.01Hz after 30 days. During the 30-day immersion, the impedance modulus $|Z|_{0.01}$Hz decreased by only 13.6%, while the phase angle at mid-frequencies remained stable around −78° to −80°, indicating retention of the coating's dielectric shielding capacity. The limited decline in Rct (<15%) further supports minimal electrolyte penetration and validates the coating's long-term barrier integrity.

Salt spray testing provided further evidence of the coating's excellent corrosion resistance. The surface appearance of coated samples after exposure to neutral salt spray for various durations. Surface inspection after 1000 hours in salt spray revealed no blistering, rusting, or edge creepage on the GO–$Ti_3C_2T_X$ coated samples, corresponding to a corrosion rating of 9 under ASTM D1654 criteria. In contrast, $Ti_3C_2T_X$ and GO-coated samples showed localized pitting and underfilm corrosion after 720 and 840 hours, respectively. Quantitative image analysis (ImageJ) indicated <0.5% corroded area for the composite, compared to 4.2% and 6.7% for the $Ti_3C_2T_X$ and GO coatings [36]. The corrosion rating, evaluated according to ASTM D1654, remained at 9 throughout the test period.

To elucidate the enhanced protective performance of the GO–$Ti_3C_2T_x$ composite coating, a schematic illustration (Figure 11) was developed, showing the key interfacial interactions. The abundant oxygen-containing functional groups on GO (–OH, –COOH) and $Ti_3C_2T_x$ (–OH, –O, –F terminations) facilitate strong hydrogen bonding and electrostatic attractions between the two components. Furthermore, these functional groups enhance chemical bonding with the hydroxylated steel surface, promoting robust physical anchoring and minimizing interfacial defects.

Such synergistic interactions—including hydrogen bonding, electrostatic forces, and van der Waals attraction—contribute to the formation of a densely packed, physically interlocked coating structure. These interfacial phenomena reduce microvoids and transport pathways for corrosive species, enhancing both adhesion and corrosion inhibition. The strong correlation between observed Rct values and proposed molecular interactions validates this structure-function relationship. This mechanistic understanding aligns with the observed improvements in mechanical robustness, electrochemical stability, and corrosion resistance.

The GO–$Ti_3C_2T_X$ composite coating significantly suppresses steel corrosion through multiple synergistic mechanisms. Firstly, the dual-lamellar structure composed of overlapping GO and $Ti_3C_2T_X$ nanosheets forms a highly tortuous diffusion pathway that hinders the penetration of water molecules and aggressive chloride ions, effectively delaying electrolyte access to the steel surface. This is evidenced by the high impedance modulus ($|Z|_{0.01}$Hz ≈ 2.3 × 10^9 Ω·cm^2) and elevated charge transfer resistance (Rct = 1.5 × 10^9 Ω·cm^2) observed in EIS measurements, indicating strong barrier behavior and minimal interfacial corrosion kinetics.

Secondly, the oxygen-containing functional groups (–OH, –COOH) on GO and surface-terminated groups (–OH, –F, –O) on $Ti_3C_2T_X$ form hydrogen bonds and electrostatic interactions not only with each other but also with the hydroxylated steel substrate. This chemical anchoring reduces coating delamination and

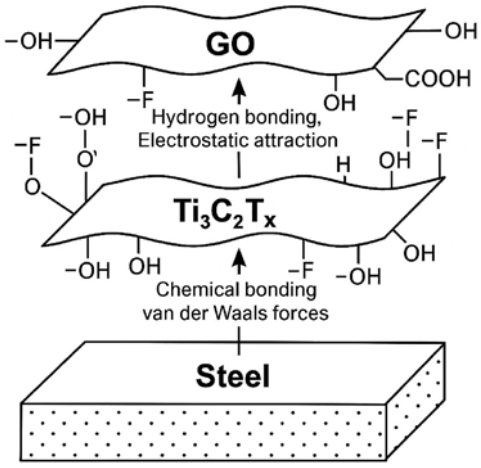

Figure 11: Schematic illustration of the interfacial interactions between GO, $Ti_3C_2T_X$, and the steel substrate. Hydrogen bonding, electrostatic attraction, and van der Waals forces facilitate strong adhesion and formation of a dense, stable coating structure.

Table 4: Comparative performance of GO–$Ti_3C_2T_X$ composite coating with similar reported coatings.

STUDY & COATING SYSTEM	HARDNESS (GPa)	ADHESION STRENGTH (MPa)	CORROSION CURRENT DENSITY (A/cm²)	SALT SPRAY DURABILITY (HOURS)	REMARKS/KEY FINDINGS
This Work: GO–$Ti_3C_2T_X$ composite	4.8 ± 0.3	18.5 ± 0.8	2.3×10^{-8}	1000	Binder-free, high adhesion and barrier performance
CAO *et al*. [18]	~3.2	14.2	~4.0×10^{-7}	720	$Ti_3C_2T_X$ multilayer coating with silane on aluminum substrate
QIANG *et al*. [4]	~3.0	15.0	~2.0×10^{-6}	800	GO-functionalized MXene for steel surface protection
ZHOU *et al*. [36]	~4.2	12.1	~1.0 × 10−7	850	Graphene oxide@ MXene hybrid in epoxy matrix

prevents underfilm corrosion. Furthermore, the moderately hydrophilic surface (contact angle ~82.5°) reduces prolonged water film formation, thus limiting electrochemical activity at the coating–substrate interface. The composite also inhibits anodic dissolution, as evidenced by the significant positive shift in corrosion potential (ΔE_{corr} = +285 mV vs. bare steel) and the three-order-of-magnitude reduction in corrosion current density (from 2.5×10^{-5} A/cm² to 2.3×10^{-8} A/cm²). Collectively, these results suggest that the coating serves both as a passive physical shield and an active kinetic suppressor, thereby offering comprehensive protection against corrosion. This dual functionality is supported by earlier literature on MXene/graphene nanocomposites and validates the proposed corrosion inhibition mechanism [36].

To further highlight the performance of the GO–$Ti_3C_2T_X$ composite coating, we provide a comparative overview of similar MXene- and graphene-based anticorrosion coatings reported in recent literature. Table 4 summarizes key mechanical and electrochemical parameters, including hardness, adhesion strength, corrosion current density, and salt spray durability. This comparative analysis demonstrates that the GO–$Ti_3C_2T_X$ system developed in this study offers a highly competitive combination of durability, corrosion resistance, and mechanical robustness.

4. CONCLUSION

This study demonstrates the successful development of a novel GO–$Ti_3C_2T_x$ composite coating that exhibits superior protection for steel surfaces through synergistic integration of both materials' advantageous properties. The optimized composite coating with a 2:1 GO:$Ti_3C_2T_x$ mass ratio and 3.0–3.5 μm thickness achieved remarkable mechanical and anticorrosion properties, significantly outperforming single-component alternatives. The composite demonstrated exceptional adhesion strength of 18.5 ± 0.8 MPa, maintaining 85% of this strength after 30 days of exposure to harsh environmental conditions (95% RH, 40°C). Mechanical characterization revealed enhanced hardness (4.8 ± 0.3 GPa) and elastic modulus (78.5 ± 2.1 GPa), while electrochemical impedance spectroscopy showed impressive barrier properties with impedance modulus reaching 2.3×10^9 Ω·cm^2, approximately two orders of magnitude higher than pure $Ti_3C_2T_x$ (3.5×10^7 Ω·cm^2) or GO (1.8×10^7 Ω·cm^2) coatings. The composite coating exhibited superior corrosion resistance with a significantly reduced corrosion current density of 2.3×10^{-8} A/cm^2 and a positive shift in corrosion potential by 285 mV compared to bare steel. Long-term stability was confirmed through 1000-hour salt spray testing, where the coating maintained a high corrosion rating of 9 according to ASTM D1654, with minimal surface deterioration. Compared with previously reported MXene-based coatings on other substrates, the GO–$Ti_3C_2T_X$ system presented here delivers a higher degree of environmental stability, interfacial adhesion, and electrochemical impedance, demonstrating its novelty and practical applicability for long-term steel protection in corrosive environments. These results demonstrate the potential of GO–$Ti_3C_2T_X$ composite coatings for practical applications in steel surface protection, offering a promising solution for addressing corrosion challenges in various industrial settings.

5. ACKNOWLEDGMENTS

None.

6. BIBLIOGRAPHY

[1] BADAIK, S., NAYAK, S., AMBADE, B., *et al.*, "A novel superior corrosion resistance polyimide–MXene (PI/$Ti_3C_2T_x$) composite coating for low alloy mild steel", *Progress in Organic Coatings*, v. 200, pp. 109046, Mar. 2025. doi: http://doi.org/10.1016/j.porgcoat.2024.109046.

[2] CAO, H., "Beyond graphene and boron nitride: why MXene can be used in composite for corrosion protection on metals?", *Composites. Part B, Engineering*, v. 271, pp. 111168, Feb. 2024. doi: http://doi.org/10.1016/j.compositesb.2023.111168.

[3] NING, Y., JIAN, D., LIU, S., *et al.*, "Designing a $Ti_3C_2T_x$ MXene with long-term antioxidant stability for high-performance anti-corrosion coatings", *Carbon*, v. 202, pp. 20–30, Jan. 2023. doi: http://doi.org/10.1016/j.carbon.2022.10.042.

[4] QIANG, Y., RAN, B., LI, M., *et al.*, "GO-functionalized MXene towards superior anti-corrosion coating", *Journal of Colloid and Interface Science*, v. 642, pp. 595–603, Jul. 2023. doi: http://doi.org/10.1016/j.jcis.2023.03.167. PubMed PMID: 37028166.

[5] CAO, H., MA, X., WANG, T., *et al.*, "Graphene-like 2D $Ti_3C_2T_x$ MXene/dodecyltrimethoxysilane coating for corrosion protection on aluminum alloy by designing multilayer structure", *Diamond and Related Materials*, v. 141, pp. 110696, Jan. 2024. doi: http://doi.org/10.1016/j.diamond.2023.110696.

[6] NIE, Y., HUANG, J., MA, S., *et al.*, "MXene-hybridized silane films for metal anticorrosion and antibacterial applications", *Applied Surface Science*, v. 527, pp. 146915, Oct. 2020. doi: http://doi.org/10.1016/j.apsusc.2020.146915.

[7] AHADIPARSA, M., DEHGHANI, A., RAMEZANZADEH, M., *et al.*, "Rising of MXenes: Novel 2D-functionalized nanomaterials as a new milestone in corrosion science - a critical review", *Advances in Colloid and Interface Science*, v. 307, pp. 102730, Sep. 2022. doi: http://doi.org/10.1016/j.cis.2022.102730. PubMed PMID: 35868175.

[8] YAN, H., LI, W., LI, H., *et al.*, "Ti_3C_2 MXene nanosheets toward high-performance corrosion inhibitor for epoxy coating", *Progress in Organic Coatings*, v. 135, pp. 156–167, Oct. 2019. doi: http://doi.org/10.1016/j.porgcoat.2019.06.013.

[9] CAI, M., YAN, H., SONG, S., *et al.*, "State-of-the-art progresses for $Ti_3C_2T_x$ MXene reinforced polymer composites in corrosion and tribology aspects", *Advances in Colloid and Interface Science*, v. 309, pp. 102790, Nov. 2022. doi: http://doi.org/10.1016/j.cis.2022.102790. PubMed PMID: 36193602.

[10] LI, C., LIU, Y., YU, Q., *et al.*, "A composite coating based on $Ti_3C_2T_x$ MXene and M16 corrosion inhibitor for self-healing anti-corrosion and wear resistance", *Surface and Coatings Technology*, v. 476, pp. 130281, Jan. 2024. doi: http://doi.org/10.1016/j.surfcoat.2023.130281.

[11] ZHANG, L., SU, W., SHU, H., *et al.*, "Tuning the photoluminescence of large $Ti_3C_2T_x$ MXene flakes", *Ceramics International*, v. 45, n. 9, pp. 11468-11474, 2019. doi: http://doi.org/10.1016/j.ceramint.2019.03.014.

[12] FU, L., KARIMI-MALEH, H., "Will MXenes be the next two-dimensional material candidate for biosensing?", *Current Pharmaceutical Analysis*, v. 18, n. 6, pp. 570–573, 2022. doi: http://doi.org/10.2174/1573412918666220113111018.

[13] CAO, H., FANG, M., JIA, W., *et al.*, "Remarkable improvement of corrosion resistance of silane composite coating with Ti3C2Tx MXene on copper", *Composites. Part B, Engineering*, v. 228, pp. 109427, Jan. 2022. doi: http://doi.org/10.1016/j.compositesb.2021.109427.

[14] DING, J., ZHAO, H., YU, H., "Structure and performance insights in carbon dots-functionalized MXene-epoxy ultrathin anticorrosion coatings", *Chemical Engineering Journal*, v. 430, pp. 132838, Feb. 2022. doi: http://doi.org/10.1016/j.cej.2021.132838.

[15] SHARMA, S., KUMAR, A., EBENSO, E.E., "MXenes and MXene-based nanomaterials for corrosion protection", *Materials Letters*, v. 335, pp. 133789, Mar. 2023. doi: http://doi.org/10.1016/j.matlet.2022.133789.

[16] AMIN, I., BATYREV, E., DE VOOYS, A., *et al.*, "Covalent polymer functionalization of graphene/graphene oxide and its application as anticorrosion materials", *2D Materials*, v. 9, n. 3, pp. 032002, Jun. 2022. doi: http://doi.org/10.1088/2053-1583/ac54ee.

[17] KHORGAMI, G., ARASH HADDADI, S., OKATI, M., *et al.*, "In situ-polymerized and nano-hybridized Ti_3C_2-MXene with PDA and Zn-MOF carrying phosphate/glutamate molecules, toward the development of pH-stimuli smart anti-corrosion coating", *Chemical Engineering Journal*, v. 484, pp. 149630, Mar. 2024. doi: http://doi.org/10.1016/j.cej.2024.149630.

[18] CAO, H., MA, X., WANG, T., *et al.*, "Graphene-like 2D Ti3C2Tx MXene/dodecyltrimethoxysilane coating for corrosion protection on aluminum alloy by designing multilayer structure", *Diamond and Related Materials*, v. 141, pp. 110696, Jan. 2024. doi: http://doi.org/10.1016/j.diamond.2023.110696.

[19] KHALILZADEH, S., ZAMANI MEYMIAN, M.R., GHAFFARINEJAD, A., "Effect of radiofrequency power sputtering on silver-palladium nano-coatings for mild steel corrosion protection in 3.5% NaCl solution", *Journal of Materials Engineering and Performance*, v. 29, n. 12, pp. 8406–8413, Dec. 2020. doi: http://doi.org/10.1007/s11665-020-05269-9.

[20] VATANI, R., ZAMANI-MEYMIAN, M.-R., GHAFFARINEJAD, A., *et al.*, "Corrosion protection of CrCu alloy coating on stainless steel", *Surface and Coatings Technology*, v. 474, pp. 130106, Dec. 2023. doi: http://doi.org/10.1016/j.surfcoat.2023.130106.

[21] ZAMANI MEYMIAN, M.R., GHAFFARINEJAD, A., FAZLI, R., *et al.*, "Fabrication and characterization of bimetallic nickel-molybdenum nano-coatings for mild steel corrosion protection in 3.5% NaCl solution", *Colloids and Surfaces. A, Physicochemical and Engineering Aspects*, v. 593, pp. 124617, May. 2020. doi: http://doi.org/10.1016/j.colsurfa.2020.124617.

[22] BALASUBRAMANI, G., PALANIAPPAN, M., "Influence of acids and slurries on the properties of recycled concrete aggregates", *Matéria*, v. 30, pp. e20240682, Jan. 2025. doi: http://doi.org/10.1590/1517-7076-rmat-2024-0682.

[23] MYLAN, J., ARUNACHALAM, G., "Material- based approaches for efficient forecasting and mitigation of air pollution using advanced neural network models", *Matéria*, v. 30, pp. e20240612, Feb. 2025. doi: http://doi.org/10.1590/1517-7076-rmat-2024-0612.

[24] MACKNOJIA, A.Z., AYYAGARI, A., SHEVCHENKO, E., *et al.*, "MXene/graphene oxide nanocomposites for friction and wear reduction of rough steel surfaces", *Scientific Reports*, v. 13, n. 1, pp. 11057, Jul. 2023. doi: http://doi.org/10.1038/s41598-023-37844-0. PubMed PMID: 37422461.

[25] NAJMI, P., KESHMIRI, N., RAMEZANZADEH, M., *et al.*, "Porous 2D Ti_3C_2 MXene nanosheets sandwiched between imine-based covalent organic frameworks (COFs) for excellent corrosion protective coatings", *Chemical Engineering Journal*, v. 456, pp. 141001, Jan. 2023. doi: http://doi.org/10.1016/j.cej.2022.141001.

[26] JIA, W., CAO, H., WANG, T., *et al.*, "Electrochemical behavior and anti-corrosion property of $Ti_3C_2T_x$ MXene/LDH heterostructured coating on aluminum alloy", *Surface and Coatings Technology*, v. 463, pp. 129551, Jun. 2023. doi: http://doi.org/10.1016/j.surfcoat.2023.129551.

[27] JI, X., SEIF, A., YUQING, Z., *et al.*, "Experimental and theoretical insights on long-term corrosion protection performance of MXene Nanosheets decorated with graphene quantum dots in epoxy coatings",

Reactive & Functional Polymers, v. 199, pp. 105904, Jun. 2024. doi: http://doi.org/10.1016/j.reactfunctpolym.2024.105904.

[28] ZHAO, H., DING, J., ZHOU, M., *et al.*, "Air-stable titanium carbide MXene nanosheets for corrosion protection", *ACS Applied Nano Materials*, v. 4, n. 3, pp. 3075–3086, Mar. 2021. doi: http://doi.org/10.1021/acsanm.1c00219.

[29] AMIN, I., VAN DEN BREKEL, H., NEMANI, K., *et al.*, "$Ti_3C_2T_x$ MXene polymer composites for anticorrosion: an overview and perspective", *ACS Applied Materials & Interfaces*, v. 14, n. 38, pp. 43749–43758, Sep. 2022. doi: http://doi.org/10.1021/acsami.2c11953. PubMed PMID: 36121119.

[30] ATAIE, S.A., QASHQAY, S.M., ZAMANI-MEYMIAN, M.R., *et al.*, "Effect of substrate bias voltage on microstructure and mechanical properties of Cr-Nb-Ti-Zr-N-O ceramic thin films produced by reactive sputtering", *Coatings*, v. 13, n. 7, pp. 1141, Jul. 2023. doi: http://doi.org/10.3390/coatings13071141.

[31] ATAIE, S.A., KESHTMAND, R., ZAMANI-MEYMIAN, M.R., "Nano-mechanical properties of Cr-Zr-Nb-N medium entropy alloy films produced by reactive sputtering", *International Journal of Refractory Metals & Hard Materials*, v. 110, pp. 106006, Jan. 2023. doi: http://doi.org/10.1016/j.ijrmhm.2022.106006.

[32] RALSTON, K., BIRBILIS, N., "Effect of grain size on corrosion: a review", *Corrosion*, v. 66, n. 7, pp. 075005, 2010. doi: http://doi.org/10.5006/1.3462912.

[33] LIU, Y., YU, J., GUO, D., *et al.*, "$Ti_3C_2T_x$ MXene/graphene nanocomposites: synthesis and application in electrochemical energy storage", *Journal of Alloys and Compounds*, v. 815, pp. 152403, Jan. 2020. doi: http://doi.org/10.1016/j.jallcom.2019.152403.

[34] GAUTAM, R., MARRIWALA, N., DEVI, R., "*A review: study of Mxene and graphene together*", *Measurement: Sensors*, v. 25, pp. 100592, Feb. 2023.

[35] ZHANG, C., NICOLOSI, V., "*Graphene and MXene-based transparent conductive electrodes and supercapacitors*", *Energy Storage Materials*, v. 16, pp. 102–125, Jan. 2019. doi: http://doi.org/10.1016/j.ensm.2018.05.003.

[36] ZHOU, Z., SEIF, A., POURHASHEM, S., *et al.*, "Experimental and theoretical studies toward superior anti-corrosive nanocomposite coatings of aminosilane wrapped layer-by-layer Graphene Oxide@MXene/waterborne epoxy", *ACS Applied Materials & Interfaces*, v. 14, n. 45, pp. 51275–51290, Nov. 2022. doi: http://doi.org/10.1021/acsami.2c14145. PMid:36321761.

[37] BADAIK, S., NAYAK, S., AMBADE, B., *et al.*, "A novel superior corrosion resistance polyimide–MXene (PI/$Ti_3C_2T_x$) composite coating for low alloy mild steel", *Progress in Organic Coatings*, v. 200, pp. 109046, Mar. 2025. doi: http://doi.org/10.1016/j.porgcoat.2024.109046.

[38] PANDEY, M., DESHMUKH, K., RAMAN, A., *et al.*, "Prospects of MXene and graphene for energy storage and conversion", *Renewable & Sustainable Energy Reviews*, v. 189, pp. 114030, Jan. 2024. doi: http://doi.org/10.1016/j.rser.2023.114030.

[39] SHI, S., ZHONG, R., LI, L., *et al.*, "Ultrasound-assisted synthesis of graphene@MXene hybrid: a novel and promising material for electrochemical sensing", *Ultrasonics Sonochemistry*, v. 90, pp. 106208, Nov. 2022. doi: http://doi.org/10.1016/j.ultsonch.2022.106208. PubMed PMID: 36327920.

[40] KOSARI MEHR, A., ZAMANI MEYMIAN, M.R., KOSARI MEHR, A., "Nanoindentation and nanoscratch studies of submicron nanostructured Ti/TiCrN bilayer films deposited by RF-DC co-sputtering method", *Ceramics International*, v. 44, n. 17, pp. 21825–21834, Dec. 2018. doi: http://doi.org/10.1016/j.ceramint.2018.08.288.

[41] ZAREPOUR, A., AHMADI, S., RABIEE, N., *et al.*, "Self-healing MXene- and graphene-based composites: properties and applications", *Nano-Micro Letters*, v. 15, n. 1, pp. 100, Apr. 2023. doi: http://doi.org/10.1007/s40820-023-01074-w. PubMed PMID: 37052734.

[42] KHORGAMI, G., ARASH HADDADI, S., OKATI, M., *et al.*, "In situ-polymerized and nano-hybridized Ti_3C_2-MXene with PDA and Zn-MOF carrying phosphate/glutamate molecules, toward the development of pH-stimuli smart anti-corrosion coating", *Chemical Engineering Journal*, v. 484, pp. 149630, Mar. 2024. doi: http://doi.org/10.1016/j.cej.2024.149630.

[43] MING, X., GUO, A., ZHANG, Q., *et al.*, "3D macroscopic graphene oxide/MXene architectures for multifunctional water purification", *Carbon*, v. 167, pp. 285–295, Oct. 2020. doi: http://doi.org/10.1016/j.carbon.2020.06.023.

[44] JIN, W., JIANG, L., HAN, L., *et al.*, "Investigation of thermal conductivity enhancement of water-based graphene and graphene/MXene nanofluids", *Journal of Molecular Liquids*, v. 367, pp. 120455, Dec. 2022. doi: http://doi.org/10.1016/j.molliq.2022.120455.

[45] DU, Y.-T., KAN, X., YANG, F., *et al.*, "MXene/Graphene heterostructures as high-performance electrodes for li-ion batteries", *ACS Applied Materials & Interfaces*, v. 10, n. 38, pp. 32867-32873, Sep. 2018. doi: http://doi.org/10.1021/acsami.8b10729. PubMed PMID: 30160474.

[46] QIANG, Y., RAN, B., LI, M., *et al.*, "GO-functionalized MXene towards superior anti-corrosion coating", *Journal of Colloid and Interface Science*, v. 642, pp. 595–603, 2023. doi: http://doi.org/10.1016/j.jcis.2023.03.167. PubMed PMID: 37028166.

[47] MIRZAEE RAD, F., TAFVIZI, F., NOORBAZARGAN, H., *et al.*, "Ag-doped ZnO nanoparticles synthesized through green method using Artemisia turcomanica extract induce cytotoxicity and apoptotic activities against AGS cancer cells: an in vitro study", *Journal of Nanostructure in Chemistry*, v. 14, n. 6, pp. 403–418, Dec. 2024. doi: http://doi.org/10.1007/s40097-023-00528-2.

[48] PAN, T., CHEN, Z., ZHAO, H., "Multifunctional catalysts for industrial VOCs oxidation: adaptative active sites and synergistic oxidation effect", *Environmental Chemistry and Safety*, v. 1, n. 1, pp. 9600001–2–9600001–4, Feb. 2025. doi: http://doi.org/10.26599/ECS.2025.9600001.

[49] JIA, W., CAO, H., WANG, T., *et al.*, "Electrochemical behavior and anti-corrosion property of $Ti_3C_2T_x$ MXene/LDH heterostructured coating on aluminum alloy", *Surface and Coatings Technology*, v. 463, pp. 129551, Jun. 2023. doi: http://doi.org/10.1016/j.surfcoat.2023.129551.

DATA AVAILABILITY

The data that support the findings of this study are available from the corresponding author upon reasonable request.